

# Probing Fine-Scale Ionospheric Structure with the Very Large Array Radio Telescope

A. S. Cohen <sup>1</sup>, and H. J. A. Röttgering <sup>2</sup>

Version: January 8, 2014

## ABSTRACT

High resolution ( $\sim 1$  arcminute) astronomical imaging at low frequency ( $\leq 150$  MHz) has only recently become practical with the development of new calibration algorithms for removing ionospheric distortions. In addition to opening a new window in observational astronomy, the process of calibrating the ionospheric distortions also probes ionospheric structure in an unprecedented way. Here we explore one aspect of this new type of ionospheric measurement, the differential refraction of celestial source pairs as a function of their angular separation. This measurement probes variations in the spatial gradient of the line-of-sight total electron content (TEC) to  $\sim 10^{-3}$  TECU/km (1 TECU =  $10^{12}$  cm $^{-2}$ ) accuracy over spatial scales of under 10 km to over 100 km. We use data from the VLA Low-frequency Sky Survey (VLSS; Cohen et al. 2007), a nearly complete 74 MHz survey of the entire sky visible to the Very Large Array (VLA) telescope in Socorro, New Mexico. These data comprise over 500 hours of observations, all calibrated in a standard way. While ionospheric spatial structure varies greatly from one observation to the next, when analyzed over hundreds of hours, statistical patterns become apparent. We present a detailed characterization of how the median differential refraction depends on source pair separation, elevation and time of day. We find that elevation effects are large, but geometrically predictable and can be “removed” analytically using a “thin-shell” model of the ionosphere. We find significantly greater ionospheric spatial variations during the day than at night. These diurnal variations appear to affect the larger angular scales to a greater degree indicating that they come from disturbances on relatively larger spatial scales (100s of km, rather than 10s of km).

*Subject headings:* atmospheric effects – techniques: interferometric

---

<sup>1</sup>Naval Research Laboratory, Code 7213, Washington, DC, 20375 USA, Aaron.Cohen@nrl.navy.mil

<sup>2</sup>Leiden Observatory, Leiden University, Oort Gebouw, P.O. Box 9513, 2300 RA Leiden, The Netherlands

## 1. Introduction

The degree to which the ionosphere distorts radiation increases greatly toward low frequencies ( $\nu \leq 150$  MHz) and has been a major obstacle to the exploitation of this frequency range for high-resolution radio astronomy. Ionospheric phase variations had historically limited most low-frequency interferometers to relatively short baselines ( $\leq 3$  km) and consequently poor angular resolution and confusion-limited sensitivity. An important breakthrough occurred with the development of self-calibration (Pearson & Readhead 1984) which motivated development of a 74 MHz system on the Very Large Array (VLA - maximum baseline 35 km) radio telescope in Socorro, New Mexico (Kassim et al. 1993, 2007). However, because of significant variations of the ionospheric phase distortions across the field of view, self-calibration with the 74 MHz system was limited to just a few dozen astronomical sources that are bright enough and isolated enough to dominate their field of view. It was not until the development of the first position-dependent ionospheric correction algorithms (Cotton et al. 2004; Cotton 2005) that it became feasible to image sources near the detection limit throughout the field of view.

The ability to conduct full-field imaging at 74 MHz led to the VLA Low-frequency Sky Survey (VLSS; Cohen et al. 2007), a 74 MHz survey of the entire sky above declination  $\delta > -30^\circ$ . It was taken primarily in the VLA B-configuration which has maximum baseline lengths of about 11 km. The primary motivations for the VLSS were astronomical, and indeed ionospheric effects were a contamination to be removed from the celestial images of interest. Nevertheless, in the process of removing these “contaminations”, ionospheric measurements were produced. The  $>500$  hours of observations taken in the B-configuration for this survey constitute an unprecedented data set with which to characterize the ionosphere. This paper presents an initial look at the fine-scale ionospheric structure seen in these data with a statistical study of the differential refraction of simultaneously imaged pairs of sources. We explore what this means both for ionospheric science itself as well as for predicting the nature and degree of ionospheric distortions that will be faced by a new generation of planned low-frequency telescopes such as LOFAR <sup>1</sup>, LWA <sup>2</sup>, MWA <sup>3</sup> and the upcoming 50 MHz system on the GMRT <sup>4</sup>.

Previous studies of the ionosphere with low-frequency radio interferometers have concentrated on using measured phases from individual antennas to detect traveling ionospheric disturbances, most likely due to gravity waves (see Jacobson & Erickson (1992) and references within). This study differs from these previous studies in several important ways. First, the previous studies used Fourier analysis of the phases of individual antennas, and therefore were mainly sensitive to traveling sinusoidal ionospheric disturbances that were persistent in time. Our study uses no initial

---

<sup>1</sup><http://www.lofar.org>

<sup>2</sup><http://lwa.unm.edu>

<sup>3</sup><http://www.haystack.mit.edu/mwa>

<sup>4</sup><http://gmrt.ncra.tifr.res.in>

model of the ionospheric structure, and is sensitive to wave and non-wavelike structure, such as turbulence. Second, because these studies only measured single sources, the region of the ionosphere probed was limited to the size of the array (all lines of sight from antennas to that one source) which was 35 km for the Jacobson & Erickson (1992) study (the VLA in A-configuration). Because our study used the entire field of view, it probed a region of the ionosphere that can be well over 100 km depending on the elevation of the field. Finally, while previous studies relied on one or a few several-hour observations, this study is based on over 500 hours of observations taken over the course of several years. Thus, rather than obtaining “snapshot” views of ionospheric behavior, we were able to create an overall statistical description of typical ionospheric structure and how this depends on various factors, such as elevation and time of day.

This paper is organized as follows. Section 2 quantitatively describes the impact of the ionosphere on incoming radiation at radio frequencies, how this affects data obtained from an interferometric array, and the specific measurements that we have obtained. In Section 3 we present and analyze the differential refraction data obtained from the VLSS and its dependence on elevation and time of day. In Section 4, we discuss what conclusions can be made from the analysis of the differential refraction statistics. Finally, in Section 5 we describe the many possibilities for future ionospheric studies based on these types of measurements.

## 2. Radio Interferometric Observations through the Ionosphere

### 2.1. Ionospheric Refraction

The ionosphere causes a phase delay to incoming radio waves which is that for radiation passing through a plasma and can be approximated by:

$$\phi \approx \frac{e^2}{c m_e \nu} \int N_e(l) dl \quad (1)$$

where  $\phi$  is the phase delay in radians,  $e$  is the electron charge,  $m_e$  is the electron mass,  $c$  is the speed of light in a vacuum,  $\nu$  is the light frequency and the integral is the column density of free electrons ( $N_e(l)$ ) along the line of sight (Rybicki & Lightman 1979). For a source at zenith and referencing to the VLSS frequency of  $\nu = 74$  MHz, this can be simplified to:

$$\phi = 1.14 \times 10^2 \left( \frac{\nu}{74 \text{ MHz}} \right)^{-1} \left( \frac{\text{TEC}}{1 \text{ TECU}} \right) \quad (2)$$

where TEC stands for total electron content and a TECU (or TEC unit) is a unit of vertical electron column density equal to  $10^{12}$  electrons/cm<sup>2</sup>.

In the limit of small refraction angles (total refraction  $\leq 10^{-3}$  radians), the refracted path passes through very nearly the same ionosphere as the un-refracted path, and so the total phase delay of a single ray can be approximated by integrating the total ionospheric delay along the

original straight-line path. Therefore, a proper ray tracing is unnecessary. We follow this “small refraction angle” approximation throughout this paper.

As a radio interferometer only measures *differences* between signals received at pairs of antennas, a constant phase delay across an interferometric array will have no effect. If the phase delay is different from one antenna to another, the phase difference between the antennas produces a geometric phase delay due to the wave front coming from a different direction as seen in Figure 1. This phase delay between the paths arriving at two antennas causes an apparent position shift in the source location by an angle:

$$\theta = \frac{\lambda \Delta\phi}{2\pi B} \quad (3)$$

where  $\lambda$  is the wavelength of the light ray,  $B$  is the baseline length, and  $\Delta\phi$  is the difference in ionospheric phase delays between the two antennas. If the ionospheric phase delay varies linearly across an array of antennas, all baselines “see” the same source shift, and the only effect on the resulting image of a celestial source is that it appears shifted from its true sky position. Combining Equations 2 and 3, we can relate the gradient of the TEC along a direction  $x$  on the ground to the observed angular shift in that direction,  $\theta_x$ , by

$$\frac{d}{dx}\text{TEC} = 6.59 \times 10^{-5} \text{TECU/km} \left(\frac{\nu}{74 \text{MHz}}\right)^2 \left(\frac{\theta_x}{1''}\right). \quad (4)$$

Note the strong dependence on frequency,  $\nu$ , which explains why the ionosphere is mainly a problem for low-frequency radio observing. If the ionospheric phase delay does *not* vary linearly across the array, but also has higher order terms (curvature), the image is not only shifted, but also distorted. However, in the regime of 74 MHz VLA observations with the B-configuration (11 km array), this distortion is rarely significant except under unusual ionospheric conditions.

## 2.2. Differential Refraction

In practice, absolute positions of sources are difficult to measure because that would require differentiating between the ionospheric phases and instrumental phases during the initial calibration of the array. The instrumental phases are determined by observing a bright calibrator source, but these solutions are degenerate to a phase gradient across the array corresponding to the unknown ionospheric position offset of that calibrator source. That phase gradient does not affect astronomical observations as it is corrected in later calibration steps. But it does corrupt the measurement of ionospheric position offsets of other observed sources. Unless this effect is determined and removed, which has yet to be done, it corrupts the measurement of absolute ionospheric gradients.

What can be measured with great accuracy is the change of ionospheric phase gradients across a single field of view. While the absolute ionospheric offsets of sources in this field of view are corrupted by an arbitrary phase gradient applied in the initial calibration, the *differences* in the position shifts of two different sources in the image can be determined very accurately because the

initial corruption applies equally to both sources and so cancels out in the difference. From now on we will refer to these differences in position shifts as the “differential refraction” between pairs of sources measured simultaneously in the same field of view. Source pair differential refraction measures the difference in the ionospheric phase gradient between the paths leading to the two source locations.

### 2.3. What Differential Refraction Measures

At this point it is useful to relate differential refraction to the geometry of the ionosphere. The diffraction-limited field of view at 74 MHz for the 25-meter VLA antenna dishes is about  $15^\circ$  across. While this field of view probes a cone-shaped region through the ionosphere, most of the electrons are usually located within a relatively thin layer near the altitude of maximum electron density in the F-layer (Kelley 1989; Schunk & Nagy 2000). It is therefore instructive to consider a thin-shell model of the ionosphere, in which the ionosphere is approximated as a very thin layer at a constant height above the Earth. For a shell height of 400 km (see Section 3.3), the field of view cone intersects the shell in a circle of diameter  $\sim 100$  km at zenith. In the 11 km B-configuration, the lines of sight from individual VLA antennas toward any single source define a set of pierce points in an 11 km region corresponding to the VLA projected to the F-layer altitude (Figure 2). The observed position offset of that source is determined by the average ionospheric phase gradient in that set of pierce points. The assumption that for individual sources ionospheric distortions are primarily refractive is equivalent to assuming that in any 11 km region of pierce points, the ionospheric variations can be approximated as linear. However, this refraction, or phase gradient, may be different at the location of another 11 km region towards a different source in that field of view, and thus the refraction across the field of view changes and the image becomes “warped”. Differential refraction measures the magnitude of the vector difference in ionospheric phase gradients between the ionospheric pierce points towards two celestial sources.

Measuring differential refraction rather than absolute refraction may seem like a major limitation. However, the differential refraction of source pairs is actually more relevant to the unique problems of high-resolution low-frequency radio imaging than the absolute refraction of an image. This is because any constant refraction across the field of view causes nothing more than a constant position shift of the entire image, which is easy to correct and remove using existing calibration techniques (such as self-calibration) commonly used at higher frequencies ( $\geq 1$  GHz). The *differences* in the ionospheric phase gradient cause the refraction to vary throughout the field of view causing a stretching or “warping” of the image which standard self-calibration cannot correct. Additionally, this warping is time-variable on a timescale of minutes or less at sub-arcminute resolution. It is this warping of the field that will be the major challenge for future low-frequency instruments to handle, and differential refraction measurements probe this effect directly.

As for studying the ionosphere, the absolute refraction corresponds to an overall TEC gradient across the entire  $\sim 100$  km field of view. Differential refraction measures higher order structure in

addition to that overall gradient. To be limited to differential refraction is to be sensitive only to finer-scale structural variations than the roughly 100 km field of view. Larger scale TEC variations can be explored by current techniques such as line-of-sight TEC measurements from ground or space-based GPS receivers, UV limb scans of recombination emission, radar and ionosonde. Radio interferometers therefore can extend the measurement of ionospheric structure to much smaller spatial scales than are currently possible.

### 3. Differential Refraction Statistics

#### 3.1. The Data

Ionospheric calibration for the VLSS was done by measuring the relative position shifts of all sources in the field of view that are detected within a 1-2 minute time interval. That time interval has been determined empirically as the maximum length of time during which time variations in the source shifts are small compared to the synthesized beam. The synthesized beam for the VLSS has a full-width at half maximum of  $80''$  ( $3.9 \times 10^{-4}$  radians) which corresponds to a physical size of about 160 meters at a zenith height of 400 km. A two-dimensional “phase screen” of ionospheric variations is fit to the position shifts of the detected sources for each time interval. The corrections are applied in the image plane. This method is called “field-based” calibration (Cotton et al. 2004; Cotton 2005) and its specific implementation for the VLSS is described in detail in Cohen et al. (2007). This calibration method works remarkably well for the 74 MHz VLA in most circumstances, producing high quality images that are astrometrically accurate within about 1/4 of a synthesized beam-width and with a typical ionospheric smearing that averages only about 1/10 of a synthesized beam-width. For some fraction of the time, the ionosphere was so turbulent that either it was impossible to image the the bright calibrator sources or it was impossible to fit a 2nd order Zernike polynomial to the source offsets. This was typically 10-20% of the total observing time.

The data set used for this ionospheric study consists of the position offset measurements for bright ( $\geq 3 Jy^5$ ) and compact sources in the field of view that were taken and recorded during the field-based ionospheric calibration of all VLSS data acquired in the 11 km B-configuration. This resulted in a list of source position offsets for roughly 3-8 sources for each 2-minute interval in over 500 hours of observing time. In addition to position offsets, the fitted peak brightnesses and integrated flux densities for each calibrator source were also recorded. The time of day was also recorded for each time interval, and from this and the source positions the elevation above the horizon was calculated.

Some radio sources are bright enough that their side-lobes can contaminate the detection of calibrator sources. For this reason, we did not use field pointings within  $15^\circ$  of Cassiopeia A or

---

<sup>5</sup>A Jy (Jansky) refers to the unit of flux density such that  $1 \text{ Jansky} = 10^{-26} \text{ W Hz}^{-1} \text{ sr}^{-1}$ .

Cygnus A, or within  $8^\circ$  of Hydra A, the Crab, Virgo A or Hercules A. In order to remove false source detections and improve the accuracy of the position offset measurements used, we restricted our study to sources within  $9^\circ$  of the field center, with fitted peak brightnesses above 4 Jy/beam<sup>6</sup> that were less than  $300''$  from their known locations. After applying these restrictions, there were 16,032 usable 2-minute time intervals in the survey. During these time intervals there were 96,575 source detections, and 299,359 pairs of simultaneous source detections.

We can estimate the position error along each axis by using the results of Condon (1997) applied to the case where we have (1) a point source, (2) a circular synthesized beam, and (3) the full-width half maximum of the Gaussian noise correlation function equal to that of the synthesized beam. This results in a position error estimate of:

$$\sigma_{pos} = \frac{\theta_b}{r \sqrt{8 \ln(2)}} \quad (5)$$

where  $r$  is the signal-to-noise ratio of the detection, and  $\theta_b$  is the full-width half maximum of the synthesized beam. Because the average RMS noise level in the 2-minute snapshot images is about  $\sim 0.6$  Jy/beam, the 4 Jy/beam brightness cutoff ensures that we used sources detected with signal-to-noise ratios of 6.67 or better. Applying Equation 5 then indicates that the predicted position errors are  $5.1''$  or less.

### 3.2. Characterizing the Differential Refraction

For each pair of simultaneous source detections we calculated the magnitude of their differential refraction as:

$$r_{ij} = |\vec{r}_{ij}| = |\vec{r}_i - \vec{r}_j| \quad (6)$$

where  $\vec{r}_i$  and  $\vec{r}_j$  are the measured vector position offsets of sources  $i$  and  $j$  with respect to their known positions taken from the higher frequency (1.4 GHz) Northern VLA Sky Survey (NVSS; Condon et al. 1998) and  $\vec{r}_{ij}$  is the vector difference between  $\vec{r}_i$  and  $\vec{r}_j$ . If the two components of the vector  $\vec{r}_{ij}$  were independent and normally (Gaussian) distributed with RMS of  $\sigma$ , the magnitude,  $r_{ij}$ , would have a Rayleigh distribution described by the following probability density function:

$$P(r_{ij}|\sigma) = \frac{r_{ij}}{\sigma^2} \exp\left(\frac{-r_{ij}^2}{2\sigma^2}\right). \quad (7)$$

To measure the actual probability distribution of  $r_{ij}$ , we needed to avoid variations in  $r_{ij}$  caused by source pair angular separation and elevation. Therefore, we considered source pairs with angular separations in the narrow range between  $5^\circ$  and  $5.5^\circ$  and only elevations higher than  $60^\circ$

---

<sup>6</sup>Units of Jy/beam refer to Janskys (1 Jansky =  $10^{-26} \text{ W Hz}^{-1} \text{ sr}^{-1}$ ) per synthesized beam.

above the horizon, where elevation effects should be small. There were 6,387 such pairs of sources, and their distribution of  $r_{ij}$  is shown as the histogram in Figure 3. Also plotted in Figure 3 as the smooth solid line is the best fitting Rayleigh distribution. Clearly, the Rayleigh distribution is a poor fit, mostly because of the relatively greater number of very high values of  $r_{ij}$  which extend into a very long “tail” which persists at a non-negligible level for well past 10 times the peak of the distribution. (This, of course also results in a corresponding deficit of values within the main peak of the distribution.) This indicates that the components of the two-dimensional vector  $\vec{r}_{ij}$  are not normally (Gaussian) distributed, but rather have a statistical overabundance of very high values, presumably corresponding to times of unusually disturbed ionospheric conditions. These very high values of  $r_{ij}$  constitute a small fraction of the data and so have relatively little effect on the median value of  $r_{ij}$ . However, because those values of  $r_{ij}$  are so high, they have a more significant effect on the mean value of  $r_{ij}$ . Indeed the mean value of  $r_{ij}$  for the distribution in Figure 3 is  $33.1''$ , which is a full 72% higher than the median value of  $19.2''$ . For a Rayleigh distribution the mean and median are  $\sqrt{\pi/2}\sigma$  and  $\sqrt{\ln 4}\sigma$  respectively, which differ by only 6%. Our goal is to measure *typical* ionospheric conditions. Therefore the median value of  $r_{ij}$ , which is less affected by a small number of extreme events, is the more robust measurement, and that is what we use for all further analysis. We define the term  $D(\theta_{ij})$  to be the median magnitude ( $r_{ij}$ ) of differential refraction for sources with angular separation of  $\theta_{ij}$ .

There is no analytical formula for the standard deviation in the median value of a non-standard distribution. However, if we assume that the standard deviation is proportional to  $N^{-1/2}$  (where  $N$  is the number of source pairs) and to the median differential shift we have:

$$\sigma(D(\theta_{ij})) = A \frac{D(\theta_{ij})}{\sqrt{N}} \quad (8)$$

where  $A$  is a constant of proportionality. We can determine  $A$  by further examining the sample in the previous paragraph. We can estimate  $\sigma(D(\theta_{ij}))$  for this case by taking random samples of  $N = 1000$  source pairs from the overall sample of 6,387 source pairs and measuring the variance in the resulting medians. Taking 10,000 such sub-samples, we get a RMS variation in the median differential refraction of  $\sigma(D(\theta_{ij})) = 0.76''$ . We already know that  $D(\theta_{ij}) = 19.2''$ , and can solve for the remaining variable,  $A = 1.25$ .

We estimate  $D(\theta_{ij})$  itself by binning the source pairs according to angular separation, taking the median value of the magnitude of the differential shifts. The errors are then calculated according to Equation 8. The resulting function is shown in Figure 4. Because of the field-of-view limitations, there are relatively fewer pairs of points with large angular separations and so the error-bars are larger for the largest separations. There were pairs with separations of more than  $16^\circ$ , but not enough for meaningful statistics, so we cut off the plot at this value. Note that the median differential source shift generally increases with source separation, though the increase is slower at larger separations. Also note that the differential refraction in the limit of zero angular separation,  $D(\theta_{ij} \rightarrow 0)$ , does not appear to be zero. This can be seen more clearly in Figure 5 which plots the median differential refraction for small angular separations with smaller bins so that the trend



towards zero angular spacings can be seen more clearly. Figure 5 only shows source pairs that are at high elevation ( $\geq 60^\circ$ ) to remove most elevation effects. A linear least squares fit of the relation between angular separation and median differential refraction estimates by extrapolation a value of  $D(\theta_{ij} \rightarrow 0) = 6.467''$ .

There are two possible reasons why  $D(\theta_{ij} \rightarrow 0)$  is non-zero. First is that there are significant variations in ionospheric spatial gradients on an angular scale well below about  $0.3^\circ$ . Such an angular scale would correspond to a spatial separation of about 2 km at a characteristic ionospheric height of 400 km (see Section 3.3). But that is much smaller than the 11 km size of the VLA in B-configuration, and therefore would violate our assumption of ionospheric variations being roughly linear within the array size. If that were the case, sources would typically be significantly distorted rather than simply being refracted. This occurs in unusually bad conditions, but is not seen typically.

The second, and more likely, explanation for a non-zero value of  $D(\theta_{ij} \rightarrow 0)$  is map-noise induced errors in the position measurements of the sources. Thus, rather than tending toward zero,  $D(\theta_{ij} \rightarrow 0)$  tends to the measurement error. The measurement error can be estimated again with Equation 5. The median peak brightness for a source in our sample is 6.88 Jy/beam. The typical noise level for the two-minute snapshot observations used to measure source positions is about 0.6 Jy/beam, for a signal-to-noise ratio of  $\rho = 11.5$ . For a resolution of  $80''$ , this implies a measurement error of  $2.96''$  for each axis. A differential refraction measurement consists of four such measurements (two axes each for two sources) and so the combined error (added in quadrature) is  $5.92''$ . This estimate is less than 10% lower than what the data show, and so this explanation seems reasonable. Ultimately we are interested in the median differential refraction caused by the ionosphere, not measurement errors. Therefore, for all future analysis, we will subtract the value of  $6.467''$  in quadrature from all median differential refraction estimates.

### 3.3. Dependence on Elevation

We examined the dependence of differential refraction on elevation by splitting the data into three elevation bins as shown in Figure 6. For each elevation bin, we fit the data to a power-law function of the form:

$$D(\theta) = \beta \left( \frac{\theta}{1^\circ} \right)^\alpha \quad (9)$$

where  $\theta$  is the source-pair angular separation and  $D(\theta)$  is the median differential refraction within a bin centered on  $\theta$ . The exponent,  $\alpha$ , and scale factor,  $\beta$ , were determined by fitting a linear model to the logarithms of the data points using the least squares method. The resulting power-law fits are shown as the solid lines in Figure 6 and their parameters are listed in Table 1. As Figure 6 demonstrates, the data are fairly well described by a power law fit. It is also clear that the differential refraction increases significantly as elevation decreases.

Because elevation is mainly a geometrical effect, it should be possible to analytically “remove” its effects on the data. We do this with the commonly used “thin-shell” model of the ionosphere in which the ionosphere is approximated as very thin layer encircling the Earth at a constant height above the Earth’s surface (Lanyi & Roth 1988; Ma & Maruyama 2003). In this model, the entire ionospheric phase delay of incoming radiation occurs at the “pierce-point” where the observing path to the celestial source intersects the ionospheric shell. Generally, the shell-height above the Earth’s surface,  $h$ , is taken to be the height of maximum electron density, with values between about 300 to 500 km typically used. In particular, Nava et al. (2007) found that a shell height of  $h = 400$  km minimized errors when using the thin-shell model to convert from slant to vertical GPS TEC measurements, and we use that value for all upcoming calculations.

According to this formulation, elevations affects the measurement of differential refraction in two ways. First, it changes the relationship between the angular separation of a source pair and the spatial separation of the ionospheric pierce-points of the observing paths to those sources. We correct the observed source-pair angular separation for this by calculating the spatial pierce-point separations for each source pair based on the altitude and azimuth of each source, and converting this to the equivalent angular separation if the sources were centered at zenith. Second, elevation determines the effective path length through the ionosphere. For an angle of incidence,  $\epsilon$  (where  $\epsilon = 90^\circ$  at zenith), the effective path length through the ionosphere is increased by a factor of  $\sec(\epsilon)$ . The ionospheric phase delays also increase by this factor (see Equation 1), as does the effective gradient of the phase delays. Because sources within each pair are a few degrees apart, they have slightly different values of  $\sec(\epsilon)$ , and we used the quadratic average to convert the measured differential refraction to its predicted zenith value.

These two adjustments attempt to convert all differential refraction and angular separation measurements to what they would be if the measurement had been taken for source pairs centered at the zenith. Figure 7 shows the same data as Figure 6, but with the differential refractions converted to their zenith equivalent as described above. As can be seen by the data points and the fitted power law curves, the applied elevation adjustments have removed nearly all differences between the three elevation bins. We note that our data cover a wide range of elevations, but generally avoid elevations below  $30^\circ$  (see Figure 8) <sup>7</sup>. So it is unclear if these corrections continue to work at lower elevations however, as Figure 7 indicates, the applied corrections appear sufficient for the data used in this study. Therefore, we conclude that elevation effects can be successfully removed analytically, and we adjust all data to their zenith equivalent for all further analysis.

---

<sup>7</sup>This is because it was already known anecdotally that the ionospheric distortions are greater at low elevations, and the original goal of the observations was astronomical rather than ionospheric.

### 3.4. Dependence on Time of Day

Correcting for elevation effects allows the examination of other effects with far greater accuracy because data from a variety of elevations can now be combined to reduce greatly the statistical measurement errors. In this section we examine variations due to the time of day. It is known that the ionosphere is thicker during the day, but it is not obvious how that should affect differential refraction. To determine this, we have split the data into day (8:00 to 16:00 local solar time) and night (20:00 to 4:00) observations. The resulting plots of median differential refraction versus source pair angular separation are shown in Figure 9. Clearly, the median differential refraction is significantly greater during the day. For reference, on the right axis of this plot we have converted the differential refraction into the equivalent TEC gradient difference using Equation 4. Also, on the top axis, we give the source-pair angular separation as a spatial separation of the source-pair pierce points projected to the ionospheric F-layer altitude, taken to be 400 km.

The error bars generally reflect the quantity of data available. Less observing time was scheduled during the day than at night<sup>8</sup> as can be seen by the histogram in Figure 10. Also, the error bars are greater for the largest angular separations because these sources pairs tend to be at the edges of the fields of view where the primary antenna beam is increasingly attenuated and so fewer source pairs were detected. We also note that the time of year was not evenly sampled, with most of our observations occurring during either early spring or late fall (Figure 11).

We fit the data to a power law with the form given by Equation 9 in the same manner described in Section 3.3. For night observations, the scale factor is  $\beta = 7.26''$  and the exponent is  $\alpha = 0.497$ , while for the day observations the scale factor is  $\beta = 10.1''$  and the exponent is  $\alpha = 0.728$ . These power-law fits to the data are also plotted in Figure 9. Once again, the power law relation describes the data extremely well, with the possible exception of the largest separations during the day. In this case, the median differential refraction does not continue increasing quite as fast as the power law relation would predict. This could be caused by the fact that at such large separations, the ionosphere becomes completely uncorrelated and so further increases in the separation no longer result in increased differential refraction.

To get a better idea of how the ionospheric phase distortions vary throughout the day, we have binned the data into 2-hour intervals of local solar time and produced power-law fits to the data in each bin, the parameters of which are listed in Table 2 along with fits to the day and night observations. From these power-law fits, we predict the median differential refraction at four representative source pair angular separations of  $2^\circ$ ,  $4^\circ$ ,  $8^\circ$  and  $16^\circ$  (corresponding to F-layer spatial separations of 14, 28, 56, and 112 km respectively) as a function of local solar time (Figure 12).

---

<sup>8</sup>This was done because it was already known anecdotally that ionospheric distortions are greater during the day.

#### 4. Conclusions and Discussion

We find that the median differential refraction of pairs of celestial radio sources is well described as a power-law function of the source pair angular separation. Though this function shows a strong elevation dependence, it appears to be due almost entirely to geometrical effects as was demonstrated by the fact that relatively simple geometrical corrections virtually eliminated this dependence. The ability to “remove” elevation effects allowed us to reference all data points to their zenith-equivalent values, greatly increasing the amount of data used and therefore the accuracy of the derived statistics.

We find that the power-law relation between the angular separation of source pairs and their median differential refraction varies greatly with time of day. When comparing day and night observations, not only is the scale factor different but the exponent increases significantly during the day, from  $\alpha = 0.497$  to  $\alpha = 0.728$  (Figure 9 and Table 2). That the exponent is higher during the day indicates that the increase in ionospheric variations is proportionally greater on the larger spatial scales than on the smaller scales.

The effects of the varying exponent can be seen when examining how the median differential refraction varies in time for several representative source-pair separations as shown in Figure 12. At all angular separations, the median differential refraction increases during the day in comparison to the night. However, this increase is more dramatic for the longer angular separations. For example, the expected differential refraction for a  $2^\circ$  separation is about  $10''$  at midnight and increases by a factor of 1.5 to about  $15''$  at noon. However, at a separation of  $16^\circ$ , the expected differential refraction increases from  $25''$  at midnight to about  $80''$  at noon, which is a factor of 3.2 increase. This demonstrates again how the additional ionospheric disturbances seen in the daytime have a relatively greater affect on the longer angular spacings, indicating that they are manifested in larger-scale structure.

The fact that additional daytime ionospheric variations tend to come from predominantly large-scale structures indicates that the degree of diurnal variations depends heavily on the field of view as indicated in Figure 12. This fact may have implications for the operation of future low-frequency instruments such as LOFAR, LWA and MWA. As the diffraction-limited field of view is frequency dependent, it could be advantageous to perform higher frequency observations during the daytime, when their smaller fields of view would be affected relatively less than the larger fields of view at the lower frequencies.

Finally, the magnitude of differential refraction at the range of angular scales we have measured can be used by the designers of all future low-frequency instruments to determine the calibration needs at various frequencies, resolutions and fields of view at which each instrument is designed to operate. While we have conducted our measurements at 74 MHz, differential refraction varies with frequency in proportion to  $\nu^{-2}$  as shown in Equation 4. Therefore the measurements we have presented can easily be converted to predict typical ionospheric behavior at other frequencies.

## 5. Future Work

This paper represents just the “tip of the iceberg” in the use of low-frequency radio interferometry to characterize fine-scale ionospheric structure. As explained earlier, the data used in this study did not represent an even sampling of the time of year (Figure 11) and time during the solar cycle. With additional observations it should be possible to determine the relation between these variables and ionospheric structure as well. It is also planned to link radio interferometry data to independent ionospheric probes, such as GPS line-of-sight TEC measurements. Finally, these existing and future data can be modeled with various phenomenon such as gravity waves or turbulence to determine the physical causes of the observed ionospheric structure (Sridharan et al 2009).

## 6. Acknowledgments

Basic research in radio astronomy at the Naval Research Laboratory is supported by the office of Naval Research. The National Radio Astronomy Observatory is a facility of The National Science Foundation operated under cooperative agreement by Associated Universities, Inc. We thank Kenneth Dymond for helpful advice.

## REFERENCES

- Cohen, A. S., Lane, W. M., Cotton, W. D., Kassim, N. E., Lazio, T. J. W., Perley, R. A., Condon, J. J., & Erickson, W. C. 2007, *AJ*, 134, 1245
- Condon, J. J. 1997, *PASP*, 109, 166
- Condon, J. J., Cotton, W. D., Greisen, E. W., Yin, Q. F., Perley, R. A., Taylor, G. B., & Broderick, J. J. 1998, *AJ*, 115, 1693
- Cotton, W. D. 2005, *Astronomical Society of the Pacific Conference Series*, 345, 337
- Cotton, W. D., Condon, J. J., Perley, R. A., Kassim, N., Lazio, J., Cohen, A., Lane, W., & Erickson, W. C. 2004, *Proc. SPIE*, 5489, 180
- Jacobson, A. R., & Erickson, W. C. 1992, *A&A*, 257, 401
- Kassim, N. E., Perley, R. A., Erickson, W. C., & Dwarkanath, K. S. 1993, *AJ*, 106, 2218
- Kassim, N. E., et al. 2007, *ApJS*, 172, 686
- Kelley, M. C. 1989, “The Earth’s Ionosphere: Plasma Physics and Electrodynamics”, *International Geophysics Series*, vol 43. San Diego: Academic Press

- Lanyi, G. E., & Roth, T. 1988, *Radio Science*, 23, 483
- Ma, G., & Maruyama, T. 2003, *Annales Geophysicae*, 21, 2083
- Nava, B., Radicella, S. M., Leitinger, R., & Coisson, P. 2007, *Advances in Space Research*, 39, 1292
- Pearson, T. J., & Readhead, A. C. S. 1984, *ARA&A*, 22, 97
- Rybicki, G. B. & Lightman, A. P., “*Radiative Processes in Astrophysics*”, New York: Wiley Interscience, 1979
- Schunk, R. W. & Nagy, A. F. 2000, “*Ionospheres: Physics, Plasma Physics, and Chemistry*”, Cambridge University press, New York, NY.
- Sridharan, R., Röttgering, H., Cohen, A., van der Tol, B. 2009 (in prep)

Table 1. Power-law fits for various elevation ranges.

| Elevation Range | $\beta$ | $\alpha$ | $N_{SourcePairs}$ |
|-----------------|---------|----------|-------------------|
| 60° to 90°      | 7.49    | 0.469    | 116,190           |
| 40° to 60°      | 11.5    | 0.456    | 151,324           |
| 0° to 40°       | 20.4    | 0.444    | 31,845            |

Note. — Parameters of power-law fits (see Equation 9) to the median differential refraction for various elevation ranges. Also shown are the number of observed source pairs for each case.

Table 2. Power-law fits for various time ranges.

| Local Time Range    | $\beta$ | $\alpha$ | $N_{SourcePairs}$ |
|---------------------|---------|----------|-------------------|
| 08:00–16:00 (day)   | 10.1    | 0.728    | 37,388            |
| 20:00–04:00 (night) | 7.26    | 0.497    | 179,783           |
| 01:00–03:00         | 7.88    | 0.466    | 43,803            |
| 03:00–05:00         | 7.19    | 0.484    | 35,157            |
| 05:00–07:00         | 8.00    | 0.386    | 9,404             |
| 07:00–09:00         | 7.24    | 0.664    | 6,280             |
| 09:00–11:00         | 11.6    | 0.673    | 8,802             |
| 11:00–13:00         | 10.8    | 0.821    | 8,017             |
| 13:00–15:00         | 8.71    | 0.812    | 11,750            |
| 15:00–17:00         | 8.10    | 0.618    | 11,335            |
| 17:00–19:00         | 5.80    | 0.694    | 22,817            |
| 19:00–21:00         | 5.29    | 0.636    | 49,156            |
| 21:00–23:00         | 7.98    | 0.456    | 44,378            |
| 23:00–01:00         | 7.69    | 0.494    | 48,457            |

Note. — Parameters of power-law fits (see Equation 9) to the median differential refraction for various time ranges given in local solar time. The first two intervals are for the day and night data. Subsequently, smaller time intervals are shown throughout the day. Also shown are the number of observed source pairs for each case. All data used for the fits are converted to equivalent values at zenith.

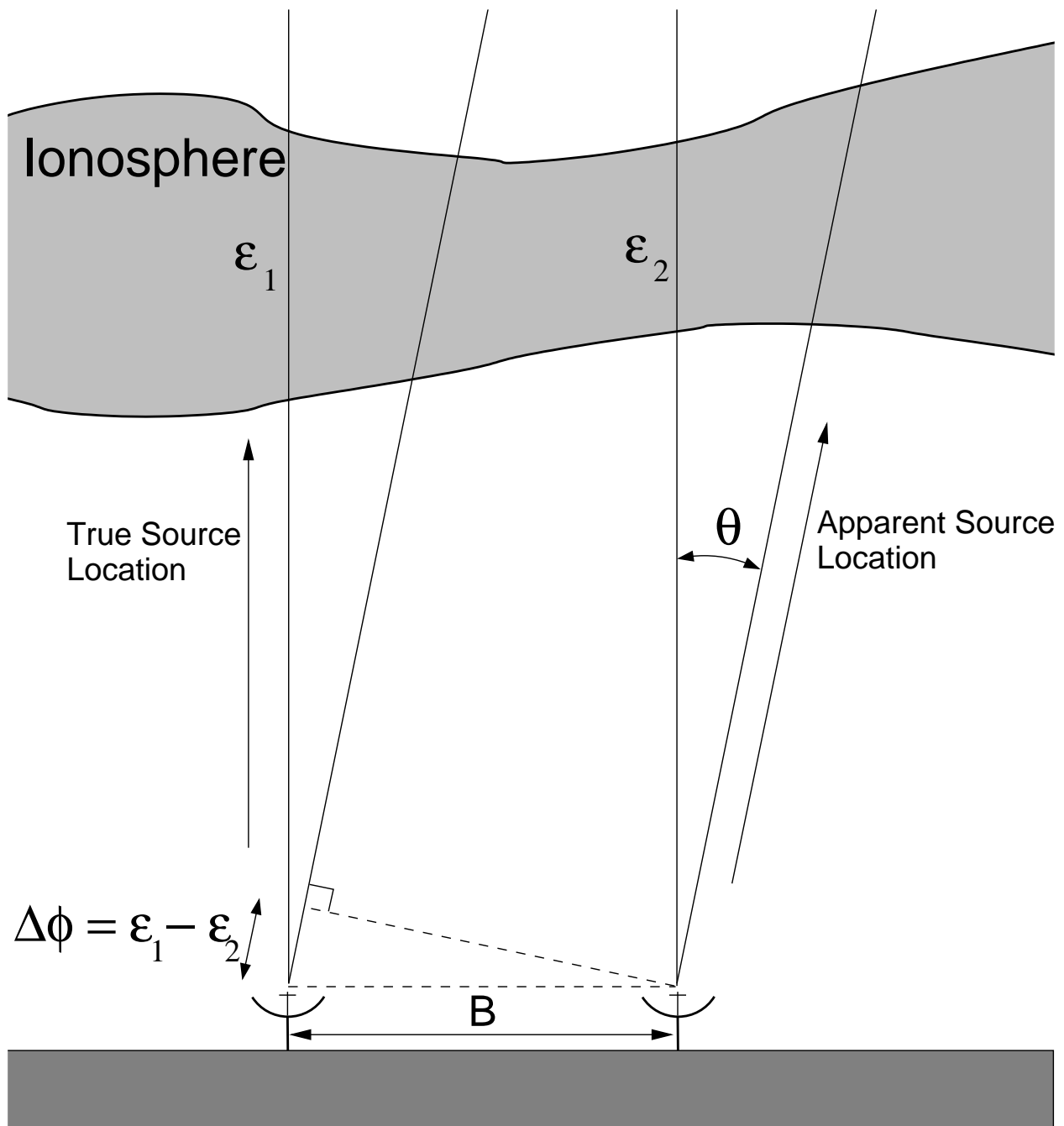


Fig. 1.— Different phase delays,  $\epsilon_1$  and  $\epsilon_2$ , between antennas are interpreted by an interferometer as a geometric phase delay,  $\Delta\phi = \epsilon_1 - \epsilon_2$ , due to the incoming signal emanating from a different direction. This assumes that the refraction angle,  $\theta$ , is small enough that the refracted paths pass through roughly the same ionosphere as the non-refracted paths and so ray tracing is not necessary.



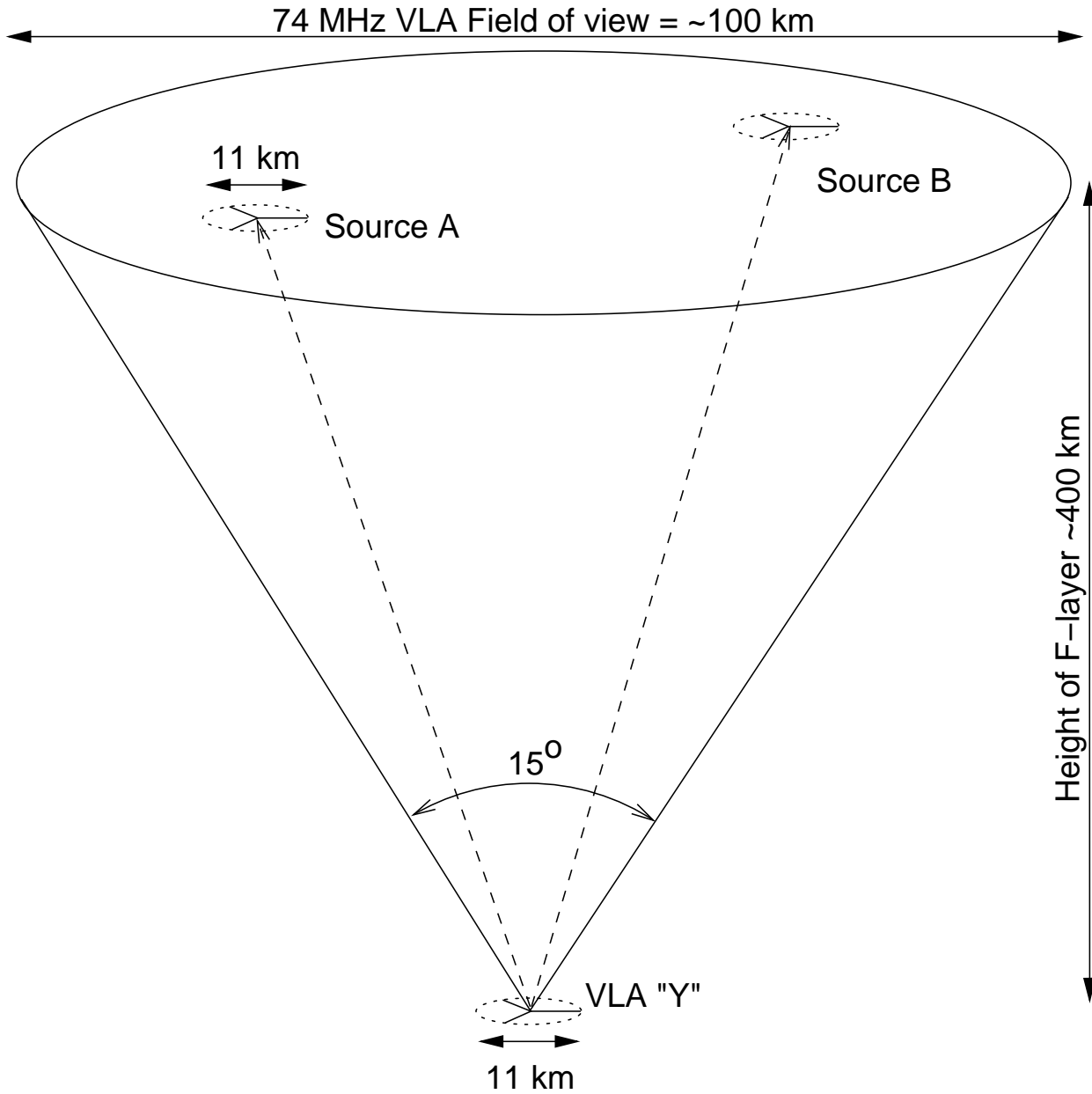


Fig. 2.— Relative sizes of the VLA in B-configuration to the field of view at 74 MHz projected to the ionospheric F-layer at a height of 400 km. In the direction of a source “A”, the relative phases through the ionosphere are measured along the 11 km projection of the VLA “Y”. For another source “B” in the field of view, the phases in a different 11 km region are measured. Within each projected region, the phases are assumed to vary linearly, though that phase gradient may be different for the two sources. The differential refraction measures the phase gradient difference between the two source locations, which probes the phase screen curvature over the field of view. All sizes in this diagram are to scale except for the vertical direction which is compressed for easier viewing.

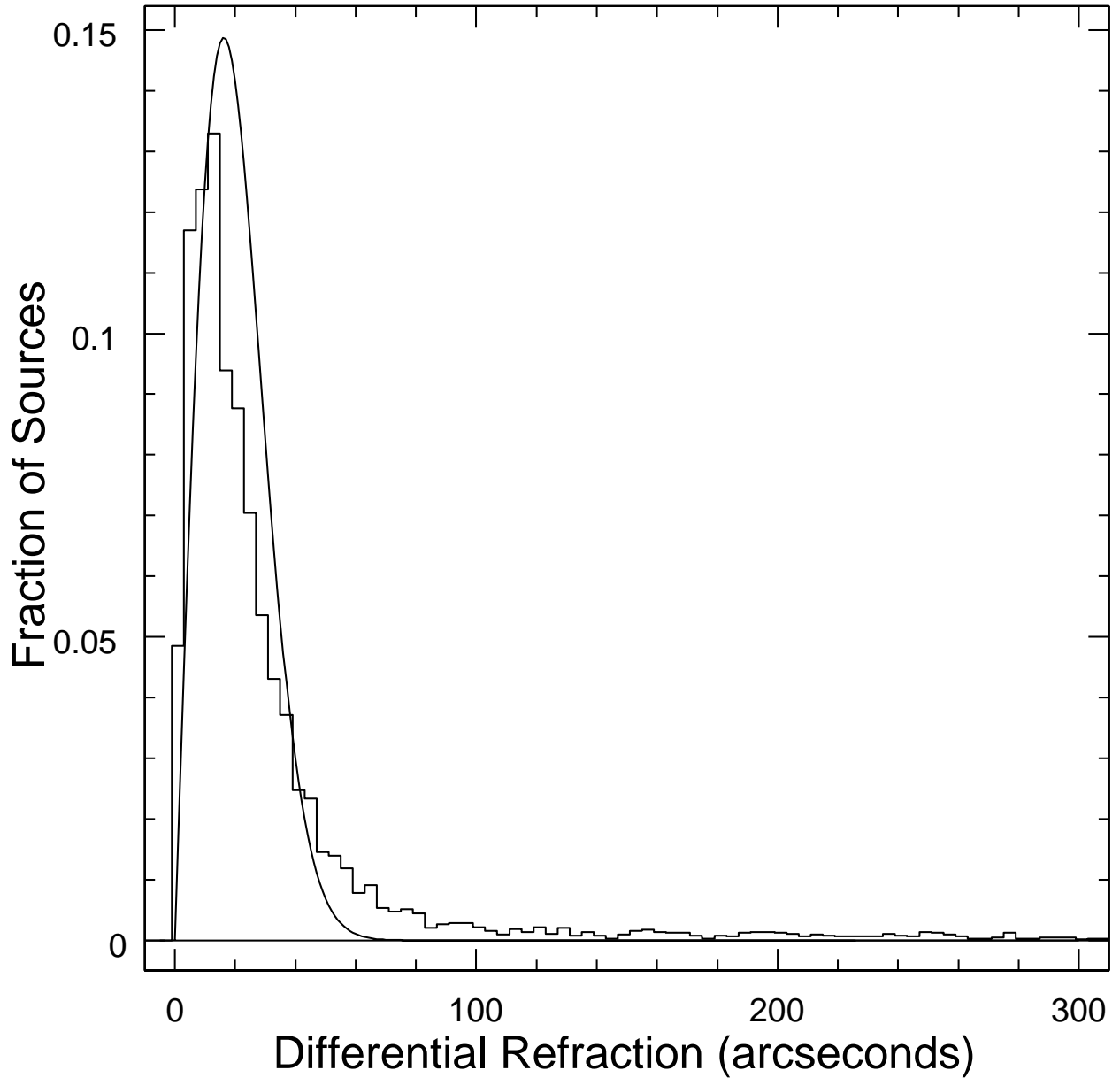


Fig. 3.— Histogram of differential refraction for all 6,387 source pairs that were separated by between  $5^\circ$  and  $5.5^\circ$  degrees, and above an elevation of  $60^\circ$  above the horizon. The best-fitting Rayleigh distribution (smooth solid line) is clearly a poor description of the actual distribution which shows relatively more data points at higher values than in the main peak. This causes the mean to be dominated by a small number of data points with very strong ionospheric distortions, and therefore be far higher than the median. For this reason, the median values of the differential refraction were used, rather than the mean values. In this case the median is  $19.2''$  while the mean is  $33.1''$ . The synthesized beam has a FWHM of  $80''$ .

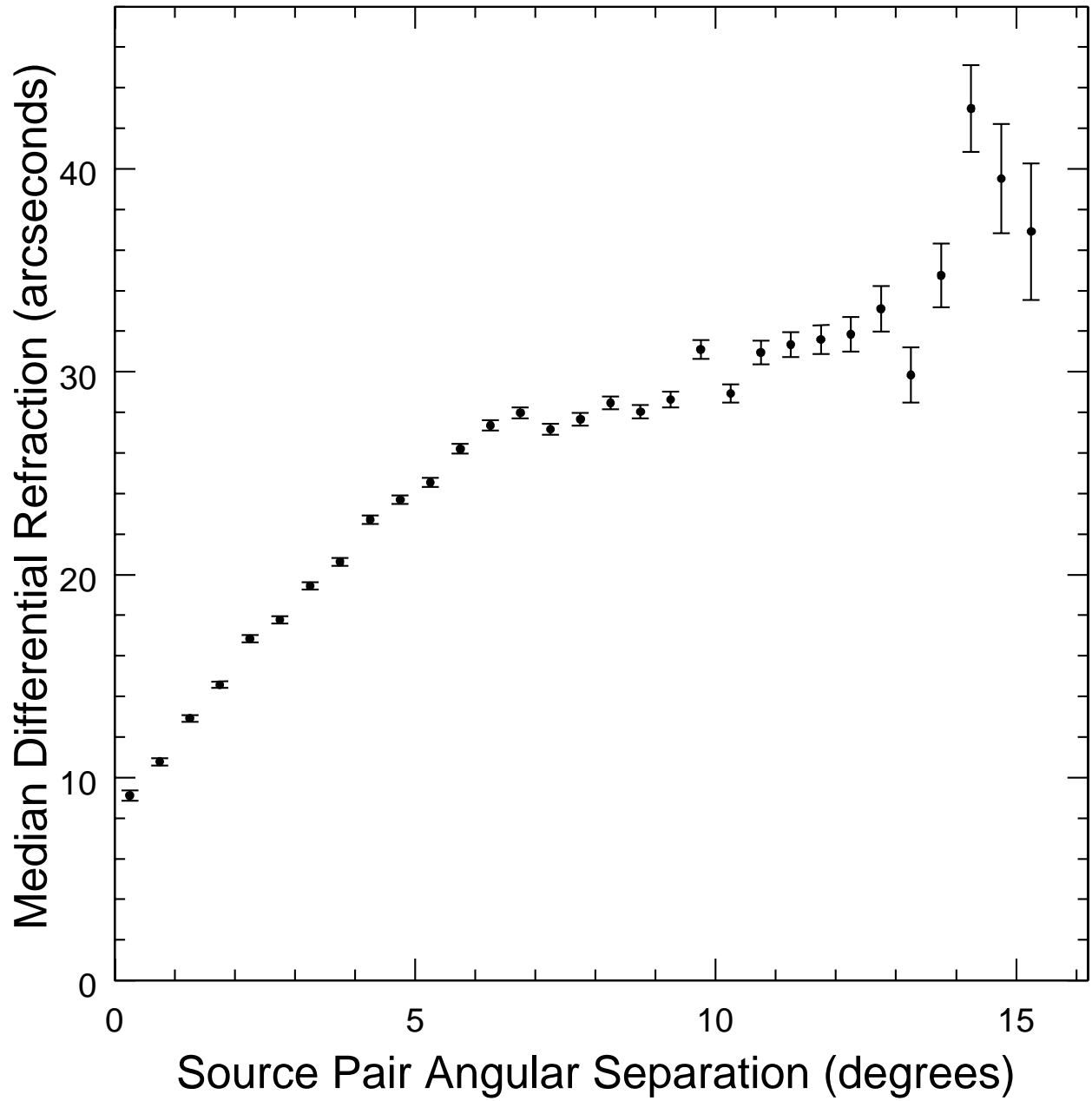


Fig. 4.— Median differential source shifts as a function of the angular separation.

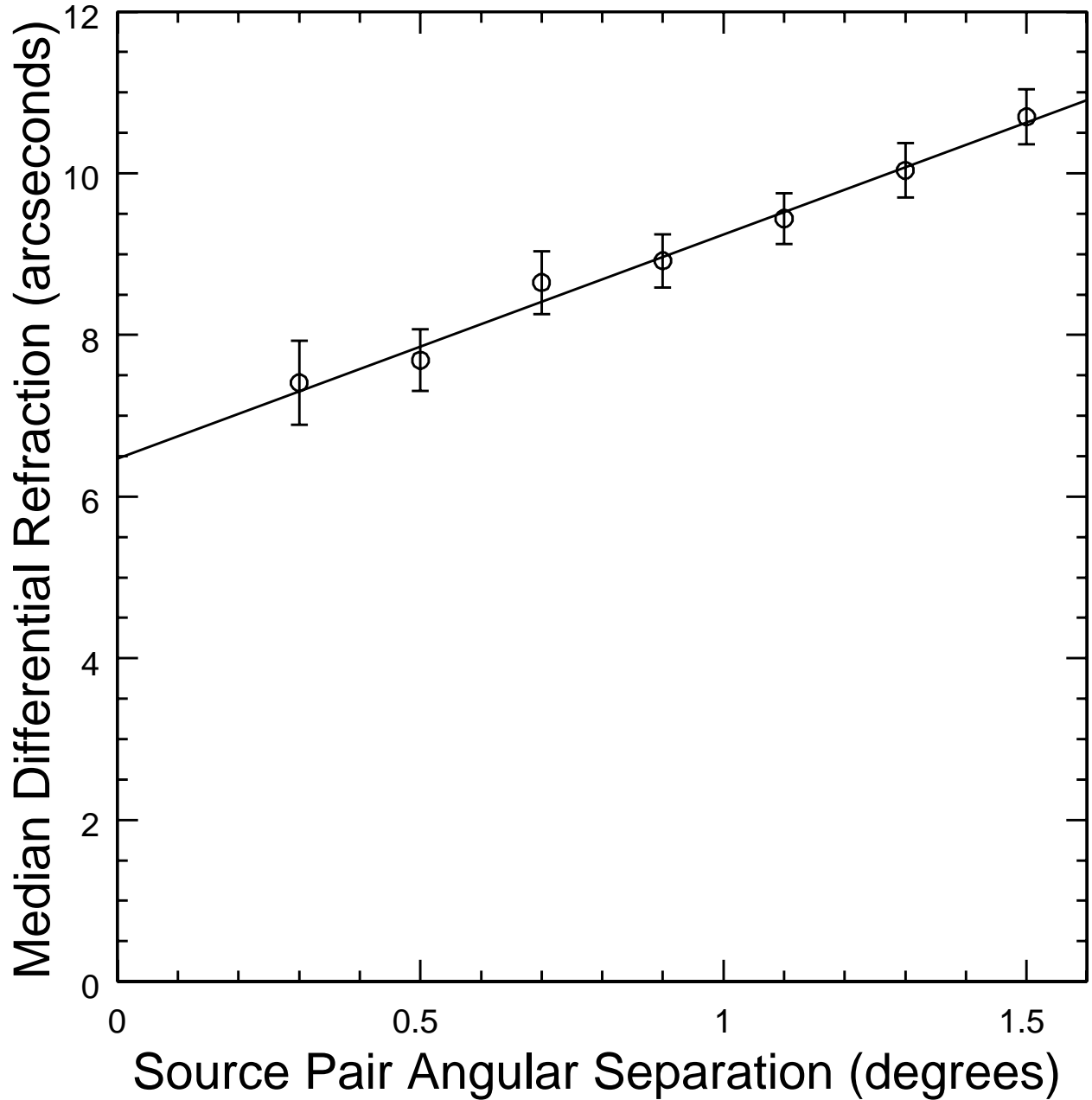


Fig. 5.— Median differential source shifts as a function of the angular separation for source pairs with small angular separations and elevations greater than  $60^\circ$  above the horizon. The solid line is a linear least-squares fit to the data points, and intersects the y-axis at a median differential refraction of  $6.467''$ .

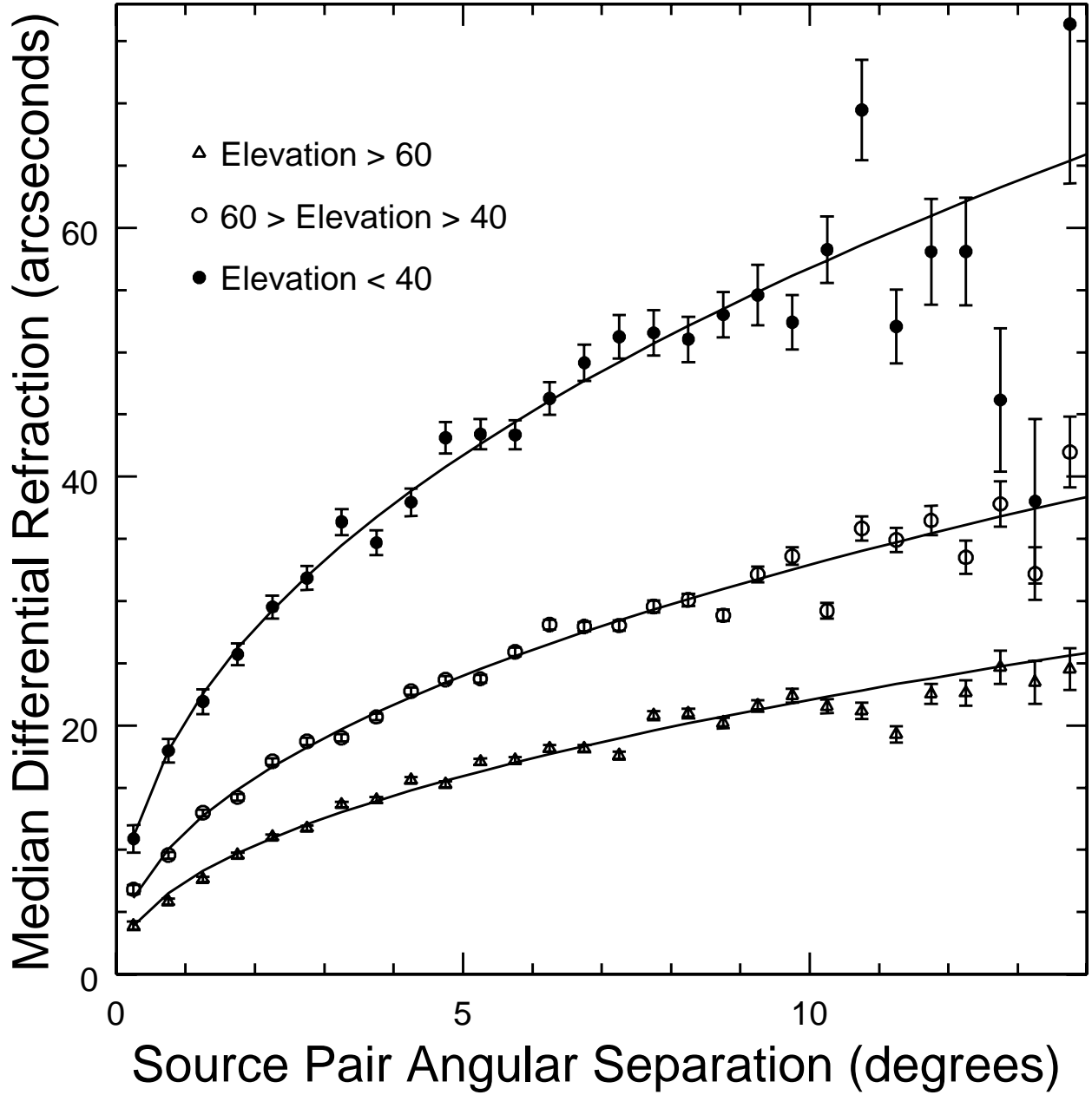


Fig. 6.— Median differential refraction as a function of source pair separation for data from three elevation bins. The solid lines show power law fits to each data set, the parameters of which are listed in Table 1.

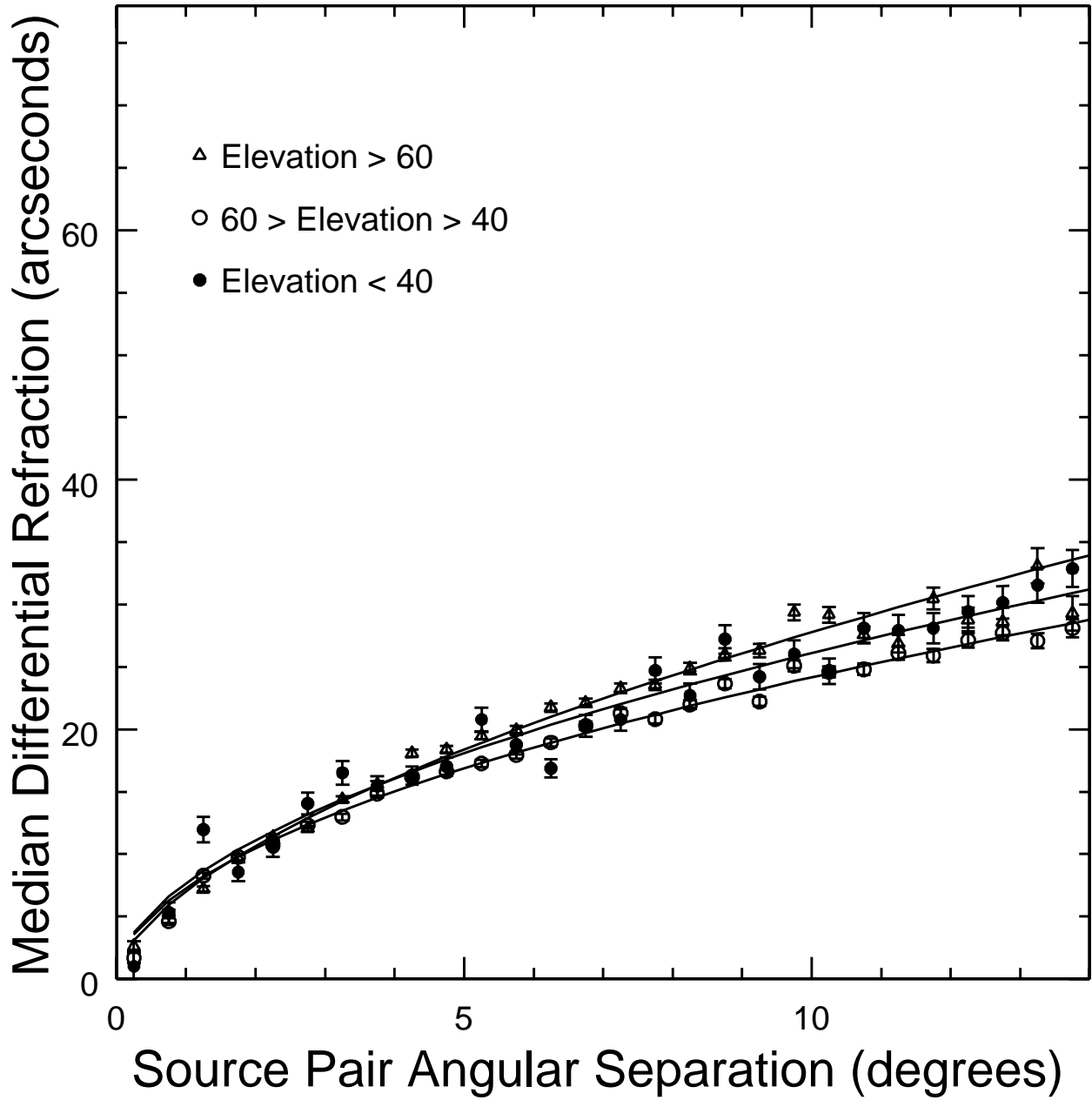


Fig. 7.— Median differential refraction as a function of source pair separation for data from three elevation bins for data converted to equivalent values at zenith.

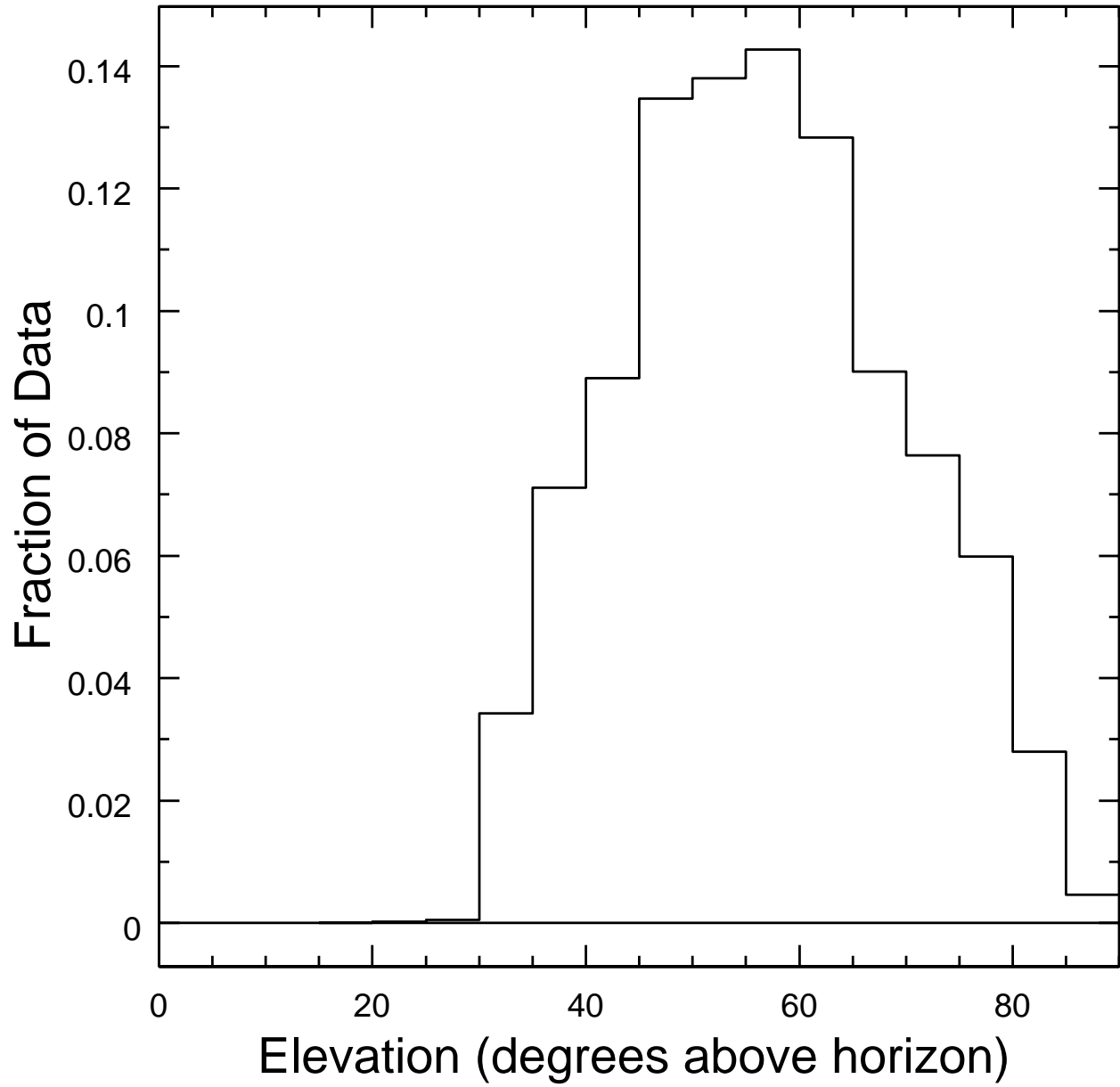


Fig. 8.— Histogram of the fraction of data taken as a function of elevation above the horizon.

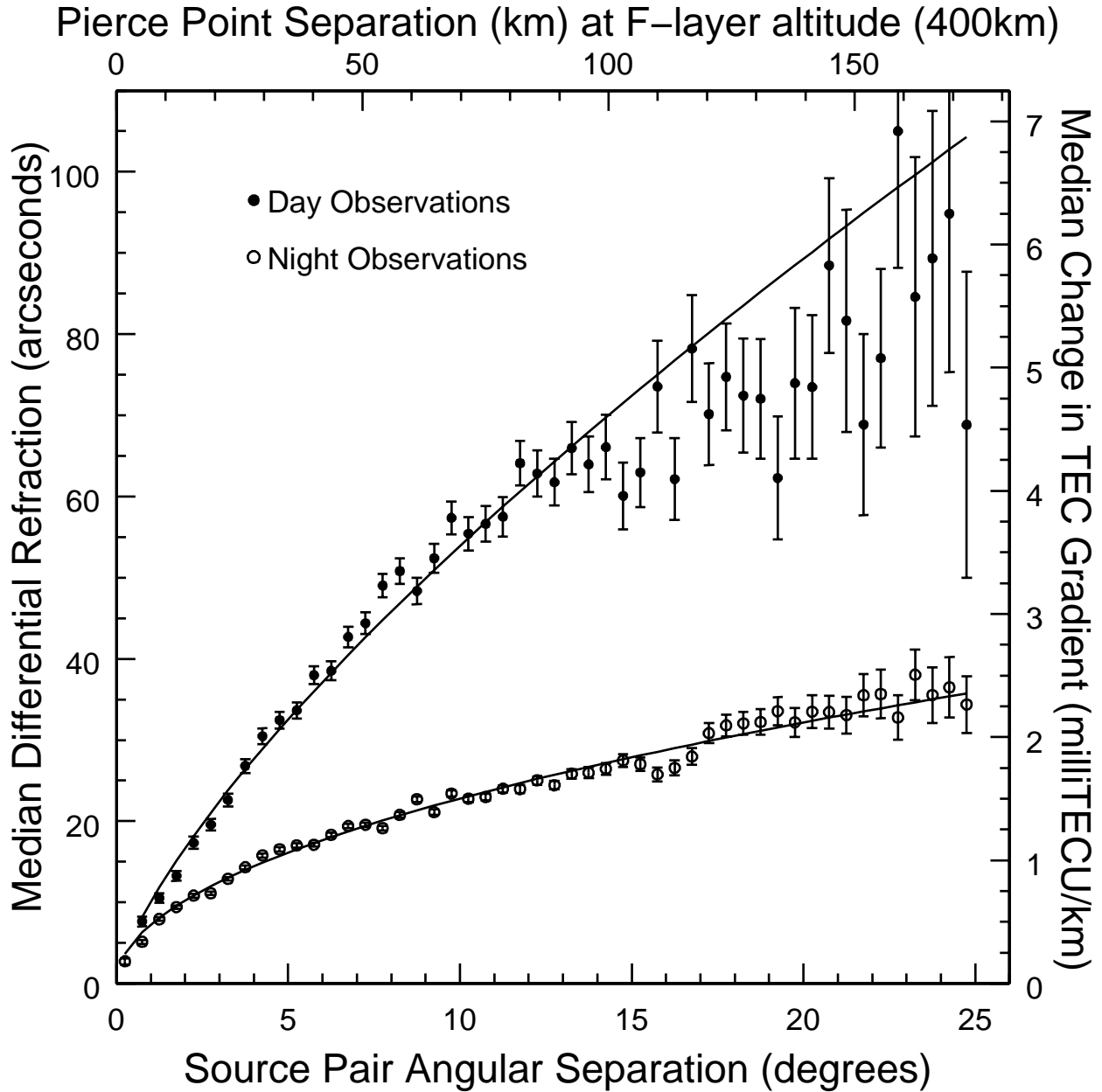


Fig. 9.— Median differential refraction as a function of source pair separation for data collected during the day and at night. All data are converted to equivalent values at zenith. The right axis shows the equivalent difference in TEC gradient between the two sources as calculated using Equation 4. The top axis shows the physical separation of the pierce points toward the two sources at the F-layer altitude taken to be 400 km.



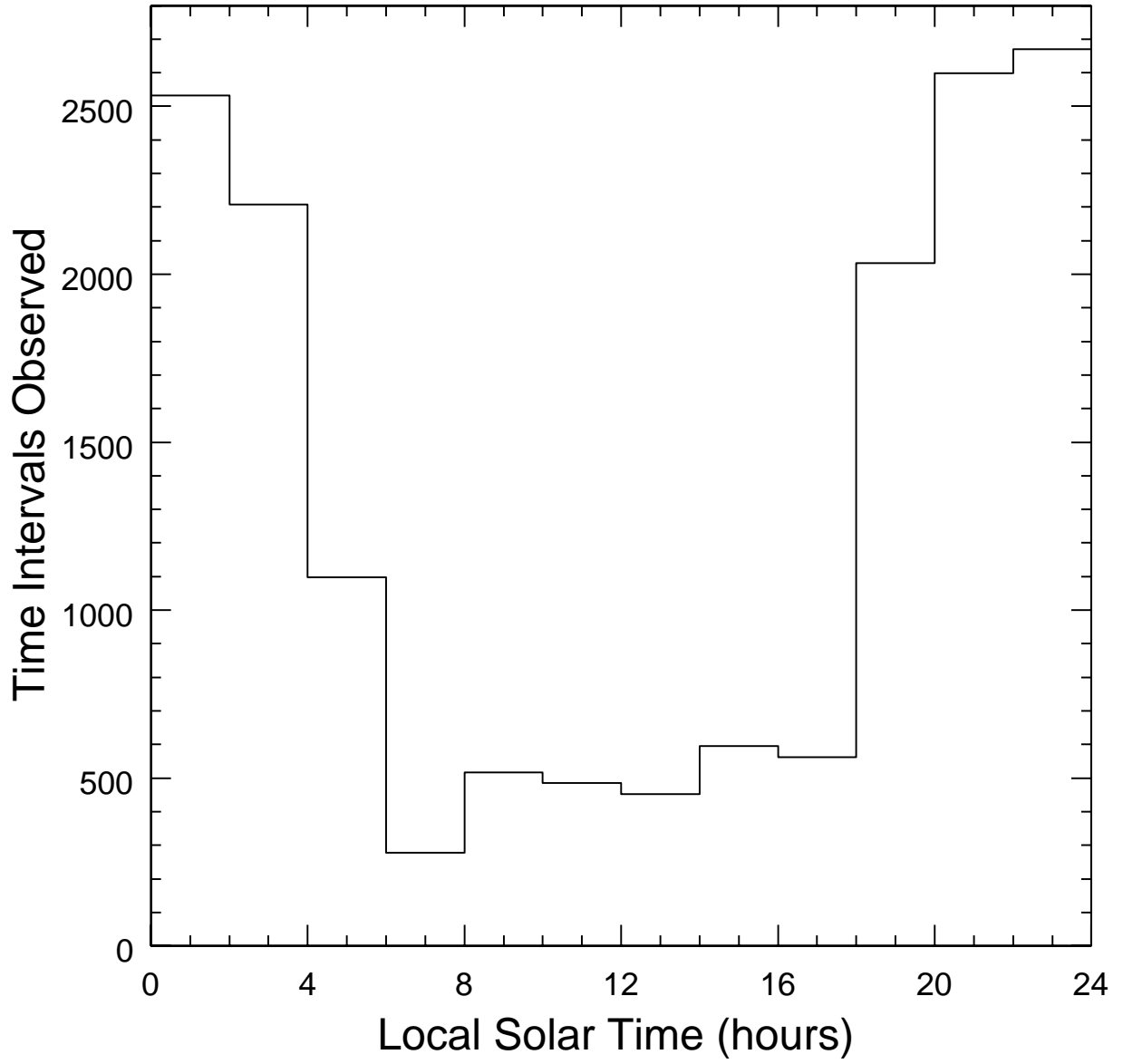


Fig. 10.— Histogram of the number of 2-minute observations conducted as a function of local solar time. Observations were done at all times, but mostly at night.

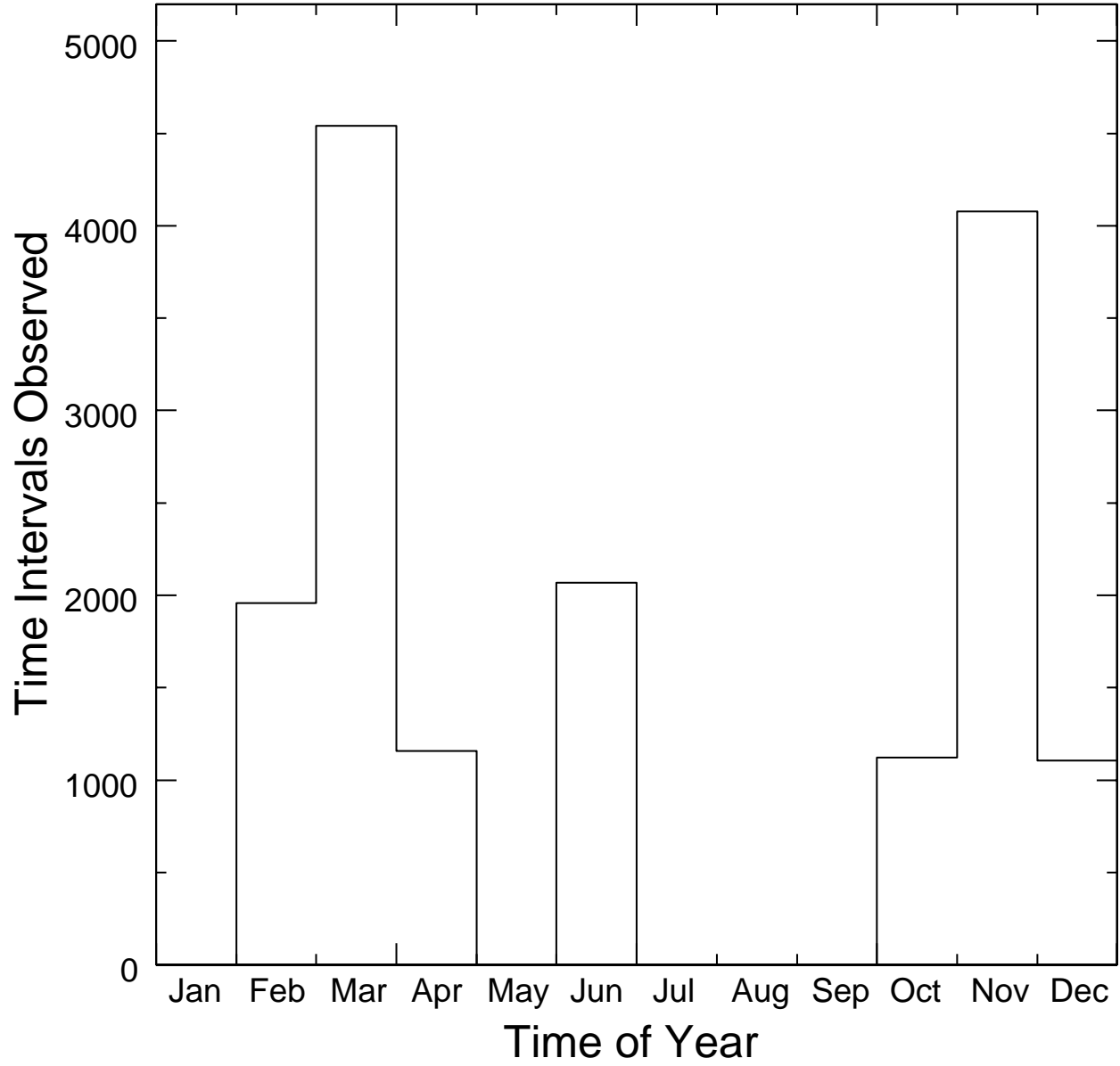


Fig. 11.— Histogram of the number of 2-minute observations conducted as a function of time of year. Because of scheduling practicalities of the VLA, the time of year is not evenly sampled, but is biased towards the early spring and late fall.

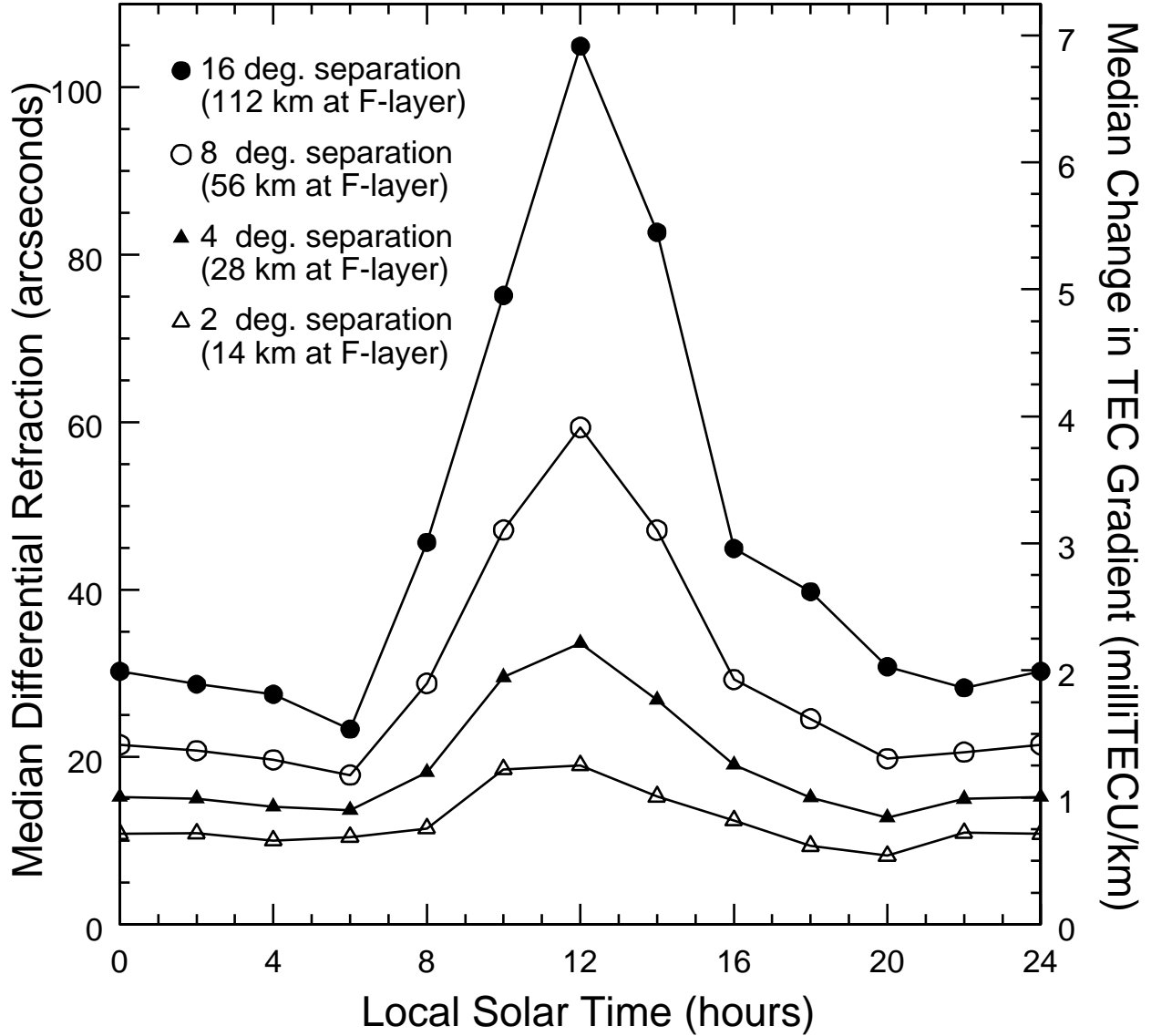


Fig. 12.— Median differential refraction as a function of local solar time for various source pair separations. All data are converted to equivalent values at zenith and are based on power law fits to the data within each time range, the parameters of which are listed in Table 2. For each source pair angular separation, the physical separation of pierce points toward the two sources at an F-layer altitude of 400 km is given in parentheses. The right axis shows the equivalent difference in TEC gradient between the two sources as calculated using Equation 4.